

Article

Feasibility Analysis of Adopting the Hydrogen Hydrostatic Thrust Bearing

Mingchen Qiang , Mingzhe Liu, Qi Zhao , Yu Hou, Shaohang Yan  and Tianwei Lai *

School of Energy and Power Engineering, Xi'an Jiaotong University, Xi'an 710049, China; yuhou@mail.xjtu.edu.cn (Y.H.)

* Correspondence: laitianwei@mail.xjtu.edu.cn; Tel.: +86-15202952214

Abstract: The hydrogen hydrostatic thrust bearing (HHTB) is a key component of hydrogen liquefaction that impacts turbo-expander characteristics. To analyze the feasibility of using the HHTB in this application, characteristics of HHTBs were calculated using a CFD model. To upgrade the performance of the HHTB, the impacts of bearing structure and operating parameters on static performance were investigated. Dynamic characteristics of the HHTB were studied using the dynamic grid method. It was found that the load capacity of the HHTB is less than that of helium-lubricated bearings but higher than that of air- and methane-lubricated bearings. The turbulent kinetic energy of hydrogen is higher than that of other gases. Load capacity can be enhanced through boosting supplied pressure, expanding the diameter of supply orifices, reducing gas film clearance, increasing the orifices quantity and setting a circumferential groove. A reduction in disturbance amplitude slightly increased the bearing's dynamic stiffness. The dynamic stability of the HHTB was improved by a small film clearance in response to disturbance.

Keywords: hydrogen hydrostatic thrust bearing; hydrogen energy; hydrogen lubrication; high-speed bearing; static characteristics; dynamic characteristics



Citation: Qiang, M.; Liu, M.; Zhao, Q.; Hou, Y.; Yan, S.; Lai, T. Feasibility Analysis of Adopting the Hydrogen Hydrostatic Thrust Bearing. *Appl. Sci.* **2023**, *13*, 9372. <https://doi.org/10.3390/app13169372>

Academic Editors: Alessandra Perna and Mariagiovanna Minutillo

Received: 25 July 2023

Revised: 12 August 2023

Accepted: 16 August 2023

Published: 18 August 2023



Copyright: © 2023 by the authors. Licensee MDPI, Basel, Switzerland. This article is an open access article distributed under the terms and conditions of the Creative Commons Attribution (CC BY) license (<https://creativecommons.org/licenses/by/4.0/>).

1. Introduction

Hydrogen is non-toxic and non-polluting, and has a low greenhouse effect, which is considered green energy [1–4]. Hydrogen energy is mainly utilized in the following applications: hydrogen internal combustion engines, fuel cells, nuclear fusion materials and solid oxide batteries. More and more attention has been paid to related technologies [5–8]. Currently, hydrogen technology is primarily focused on producing and storing hydrogen. The most economical method of storing and transporting hydrogen over long distances is currently in the form of liquid hydrogen, which requires a hydrogen liquefaction process [9–12].

In large hydrogen liquefaction systems, high-speed hydrogen turbo-machinery plays a critical role. The main equipment that has a cooling effect during the hydrogen liquefaction process is the hydrogen turbo-expander. Turbo-expander characteristics have a significant impact on the liquefaction rate and its economic efficiency [13–16].

As a result of its low viscosity and non-contamination, the gas bearing has been extensively adopted in turbo-expanders [17–19]. Based on the different directions of support force, gas bearings can be classified as journal bearings and thrust bearings. The application of gas bearings in a turbine system is presented in Figure 1.

Based on the mechanism of bearing force generation, hydrodynamic bearings and hydrostatic bearings are the two main forms of application of gas bearings [20–22]. For hydrostatic bearings, bearing load capacity is achieved by means of an external gas supply. Generally speaking, the hydrostatic bearing has better reliability, and its bearing capacity can be artificially adjusted to fit operating requirements [23–26].

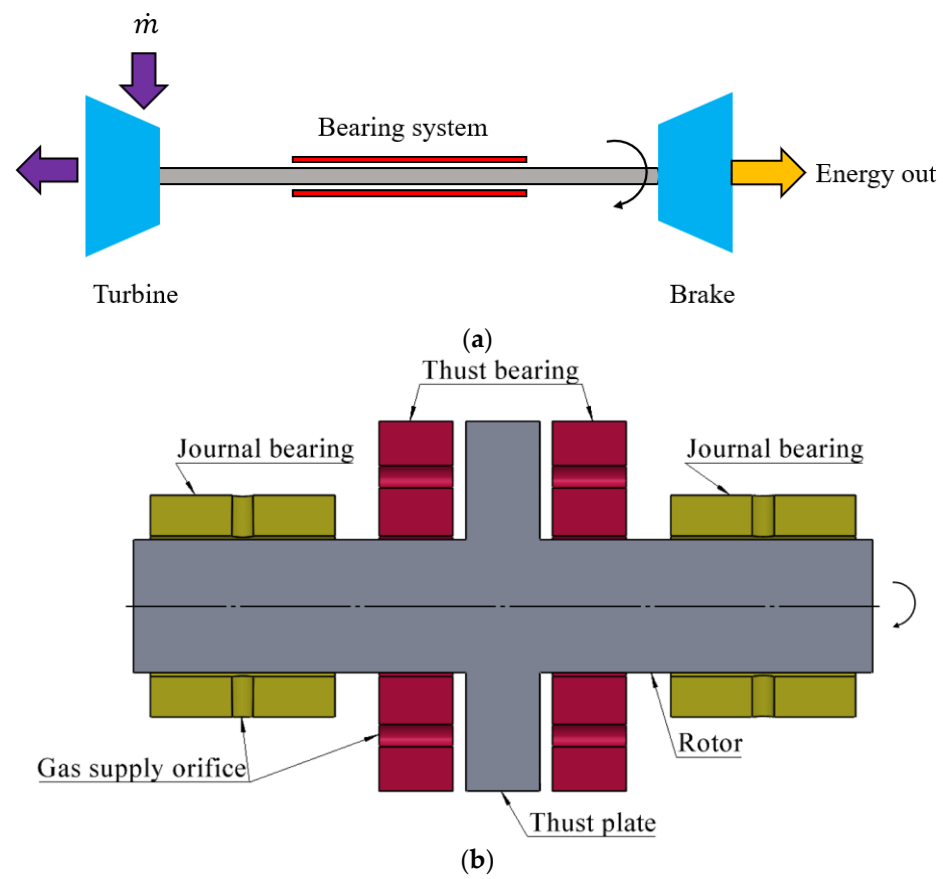


Figure 1. The application of gas bearings in a turbine system. (a) Turbine system schematic diagram. (b) Bearing system schematic diagram.

In hydrogen turbo-expanders, due to their low density, large flow rate and enthalpy difference, the axial thrust bearing capacity may not be sufficient, which may lead to mechanical failure. Therefore, research regarding thrust bearing is particularly important. Masaaki et al. carried out an extensive analysis of the impacts of small orifices on hydrostatic thrust bearing [27]. Nishio et al. verified the above research results. In addition, they conducted experimental and numerical analyses regarding the relationship between surface roughness and bearing performance. It was found that bearings with a gas orifice had better stiffness and damping coefficients compared to composite throttling [28]. Gao et al. numerically evaluated the impact of orifice structure on bearing performance under different operational conditions using a computational fluid dynamics (CFD) model. Their results showed that bearing performance was influenced by the form of the inner cavity. As film clearance decreased, some parameters, such as pressure drop, gas vortex and turbulence intensity, decreased. The bearing load capacity decreased slightly as the spindle speed increased [29]. Renn et al. conducted experiments on and simulations of mass flow characteristics in hydrostatic bearings. It was found that characteristics of the nozzle strongly influenced gas mass flow characteristics at the orifice [30]. Shi et al. studied bearing characteristics using a throttle hole based on a three-dimensional model [31]. Li et al. manufactured a bearing compensated by a porous material restrictor to enhance bearing performance; composite restrictors for optimal bearing parameters were provided [32]. Zhao et al. put forward a bearing with a flexible equalizing pressure groove according to the principle of fluid–structure coupling. Its stiffness was improved by 59%, which was validated by numerical calculation [33]. Huang et al. analyzed the impacts of speed and film clearance on pressure distribution and spindle static stiffness based on CFD models. It was found that pressure was significantly influenced by the film’s thickness. Increasing spindle speed could lead to higher pressure on the spindle surface and increased spindle

stiffness [34]. Zheng et al. investigated the hydrodynamic hammering phenomenon and performance of a concave-hole single-tile bearing. The numerical calculation showed that the delayed effect of the pressure change in the gas chamber was a decisive factor for the pneumatic hammer phenomenon [35]. Wu et al. analyzed features of pneumatic hammer self-excitation in hydrostatic bearings under different structural parameters and supplied pressures. It was found that because the flow rate and supplied pressure were larger than the corresponding critical values, gas hammer self-excitation tends to happen [36]. Sahtod et al. conducted simulations of porous and partially porous hydrostatic thrust bearings to research the effect of disturbance frequency on dynamic characteristics. It was shown that the load capacity amplitude reduced as the frequency increased. Additionally, the damping of the partially porous bearing decreased with increasing orifice quantity [37]. Wei et al. optimized the bearing design based on basic hydrodynamic equations for boosting performance [38]. Ishibashi et al. considered the influence of gas inertia force on the bearing and applied a CFD model for numerical verification and analysis [39]. Guo et al. calculated gas bearings using air, carbon dioxide, hydrogen and helium as lubricating mediums using a CFD model. It was shown that the load capacity is significantly influenced by the lubricating medium. [40]. Yan et al. investigated hydrostatic bearings lubricated using air, helium and hydrogen. Additionally, a model suitable for various lubricating media was proposed [41]. The above two studies, regarding the influence of lubricants, were founded on the laminar flow model; the influence of the flow states of lubricating mediums was not considered.

At present, most research regarding turbo-expanders is conducted using air as the working medium [42,43]. To improve bearing performance, the main structural parameters, such as the diameter of orifices, the location of orifices and the shape of gas chambers, are optimized [44,45]. As the application of hydrogen bearings is not sufficiently mature, using small orifices to supply gas to hydrostatic thrust bearings when designing thrust bearings can provide more adequate load capacity and stable performance [46]. As a result of the special physical properties of hydrogen, design standards for HHTBs have not yet been defined. In practical applications, HHTBs are often used at high pressure around the bearing, and there is a large enthalpy difference during expansion. The increase in pressure around the bearing can cause the load capacity of the HHTB to be insufficient; if this occurs, the performance of the bearing is not completely adequate for high-speed operation, which can cause the hydrogen turbo-expander to fail during operation. With the purpose of investigating the feasibility of using the HHTB in this application, the performance of bearings using hydrogen was compared with the performances of bearings using other lubricating gases using the CFD turbulence model. Factors to improve the performance of HHTB were considered. The effects of supplied pressure, supply orifice diameter, the quantity of supply orifices, circumferential groove and gas film clearance on bearing performance were evaluated. The dynamic characteristics of HHTB under harmonic disturbance with various amplitudes, frequencies and gas film equilibrium values were studied.

2. Numerical Model

2.1. Hydrogen Hydrostatic Thrust Bearing Structure

The HHTB's structure is presented in Figure 2a,b. The main parameters of the bearings include orifice diameter d , number of orifices N , groove depth h , groove width s and film clearance c_0 .

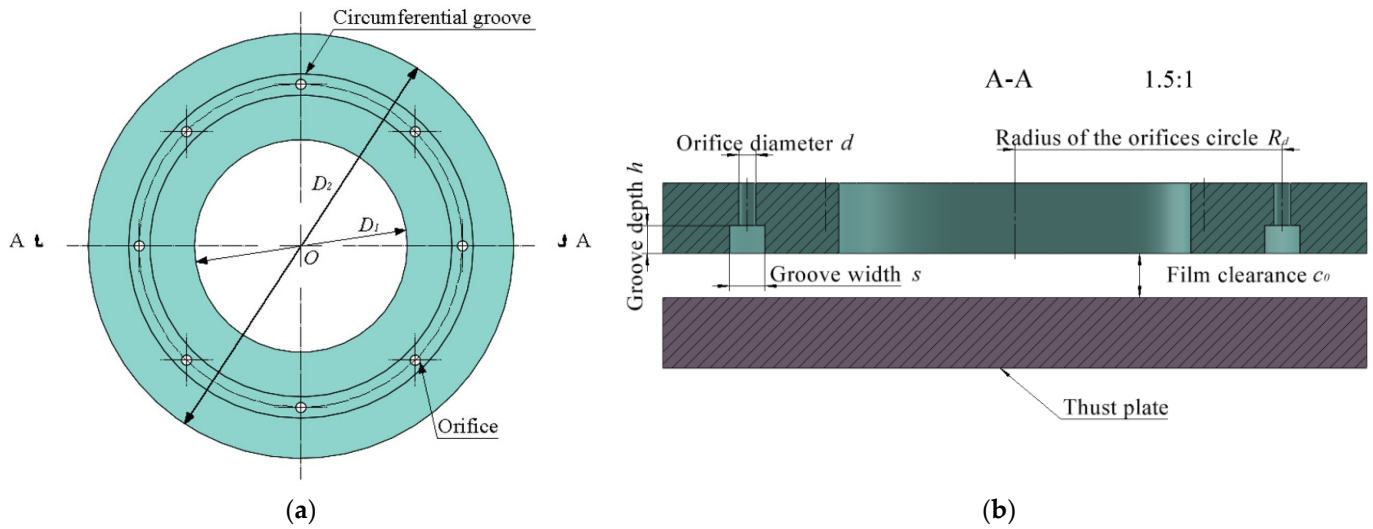


Figure 2. Hydrogen hydrostatic thrust bearing structure and simulation model: (a) front view and (b) sectional view.

2.2. Computational Model

The complete Navier–Stokes equation of three-dimensional compressible flow is numerically simulated as follows [29].

$$\rho \left(\frac{\partial u}{\partial t} + u \frac{\partial u}{\partial x} + v \frac{\partial u}{\partial y} + w \frac{\partial u}{\partial z} \right) = \rho f_x - \frac{\partial P}{\partial x} + \mu \left(\frac{\partial^2 u}{\partial x^2} + \frac{\partial^2 u}{\partial y^2} + \frac{\partial^2 u}{\partial z^2} \right) \quad (1a)$$

$$\rho \left(\frac{\partial v}{\partial t} + u \frac{\partial v}{\partial x} + v \frac{\partial v}{\partial y} + w \frac{\partial v}{\partial z} \right) = \rho f_y - \frac{\partial P}{\partial y} + \mu \left(\frac{\partial^2 v}{\partial x^2} + \frac{\partial^2 v}{\partial y^2} + \frac{\partial^2 v}{\partial z^2} \right) \quad (1b)$$

$$\rho \left(\frac{\partial w}{\partial t} + u \frac{\partial w}{\partial x} + v \frac{\partial w}{\partial y} + w \frac{\partial w}{\partial z} \right) = \rho f_z - \frac{\partial P}{\partial z} + \mu \left(\frac{\partial^2 w}{\partial x^2} + \frac{\partial^2 w}{\partial y^2} + \frac{\partial^2 w}{\partial z^2} \right) \quad (1c)$$

where, x, y and z are directional coordinates, u, v and w are velocities in the three directions, respectively, t is time, μ is dynamic viscosity, ρ is gas density, P is gas pressure and f is external force per unit volume of fluid.

Consider the following equation for the continuity of the flow.

$$\frac{\partial(\rho u)}{\partial x} + \frac{\partial(\rho v)}{\partial y} + \frac{\partial(\rho w)}{\partial z} + \frac{\partial \rho}{\partial t} = 0 \quad (2)$$

To determine the flow pattern, the Reynolds number (Re) is used. The flow regime of the gas film is regarded as turbulent if the Reynolds number is greater than 2000, and the clearance thickness is the characteristic length [47]. Re is computed as [48]:

$$Re = \frac{\omega r c_0}{\nu} \quad (3)$$

where ν is kinematic viscosity, ω is rotational speed, c_0 is film clearance, r is the radius and $r = D_1/2$. The highest Reynolds number in the gas film reached 3356 at 50,000 rpm and 0.5 MPa; the flow pattern was considered to be turbulent flow.

To explore the characteristics of the HHTB, the CFD turbulence model was computed using FLUENT®. Considering the vortex effect, a $k-\epsilon$ model was used, which could better reflect complex flows involving impingement. The flow field of an HHTB is symmetrical, and calculated according to the structure of a gas supply orifice with periodic boundaries on both sides, as displayed in Figure 3. The specific boundary conditions are defined as follows:

- (1) The pressure inlet is the supplied pressure (P_{in});
- (2) The pressure outlet is the pressure around the bearing (P_0);
- (3) Both sides of the film are periodic boundaries of the circumferential flow characteristics;
- (4) The rotational wall is the contact surface with the thrust plate;
- (5) The other walls are fixed boundaries with no sliding and no flow.

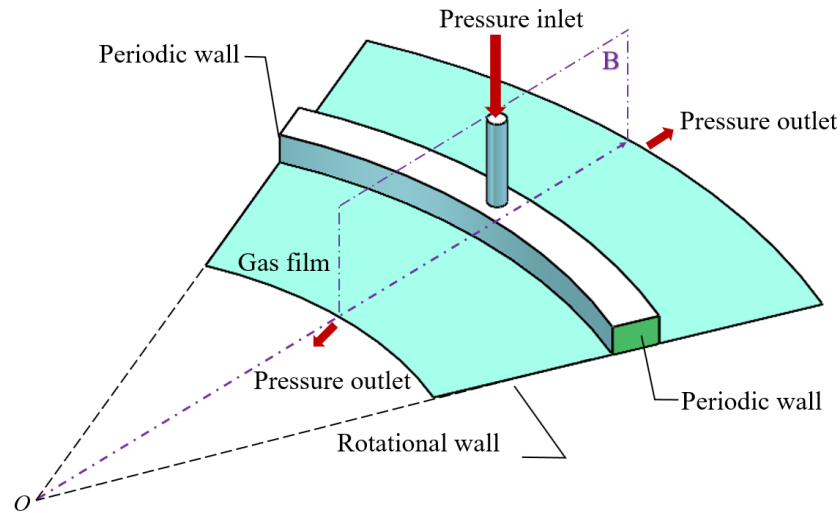


Figure 3. Computational domain and boundary conditions.

When the thrust plate is exposed to a small harmonic disturbance, the gas film clearance changes as well, which is expressed as follows:

$$\Delta c = a \cdot \sin (2\pi f t + \varphi) \tag{4}$$

where a represents amplitude, f represents disturbance frequency and φ represents the initial phase. Simultaneously, the increment of the gas film bearing capacity also has harmonic motion [49]. The dynamic grid model was adopted to realize the periodic motion of the dynamic gas film.

To comprehensively evaluate the dynamic characteristics of the HHTB, the damping dissipation energy, equivalent damping and dynamic stiffness coefficient were analyzed. The relationship between dynamic load capacity and dynamic stiffness can be formulated as follows:

$$[K] = \sum_{i=1}^n [K]^i, \{f\} = \sum_i \{f\}^e \tag{5}$$

$$[K]\{\Delta c\} = \{f\} \tag{6}$$

Equivalent damping was introduced to represent the energy dissipation capacity, as shown in the following [50]:

$$D_{eq} = \frac{2\Delta E_{dis}}{\Omega l^2} \tag{7}$$

where ΔE_{dis} is the energy dissipation (the closed area of the load capacity–film clearance curve), l is the maximum deformation of the gas film, Ω is the disturbance frequency and $\Omega = 2\pi f$.

2.3. Grid Independence and Model Validation

The evolution of bearing load capacity depending on the number of grid units is presented in Figure 4a. When the grid number was increased to 160,000, the error of the calculation results did not exceed 5%. The model computations were compared and validated using the literature [51], as shown in Figure 4b, in which the lubricating working medium is air. Parameters used in the validation calculation are shown in Table 1, as per

the literature [51]. The calculated results were well verified using the literature data, and the relative error value did not exceed 8% at maximum.

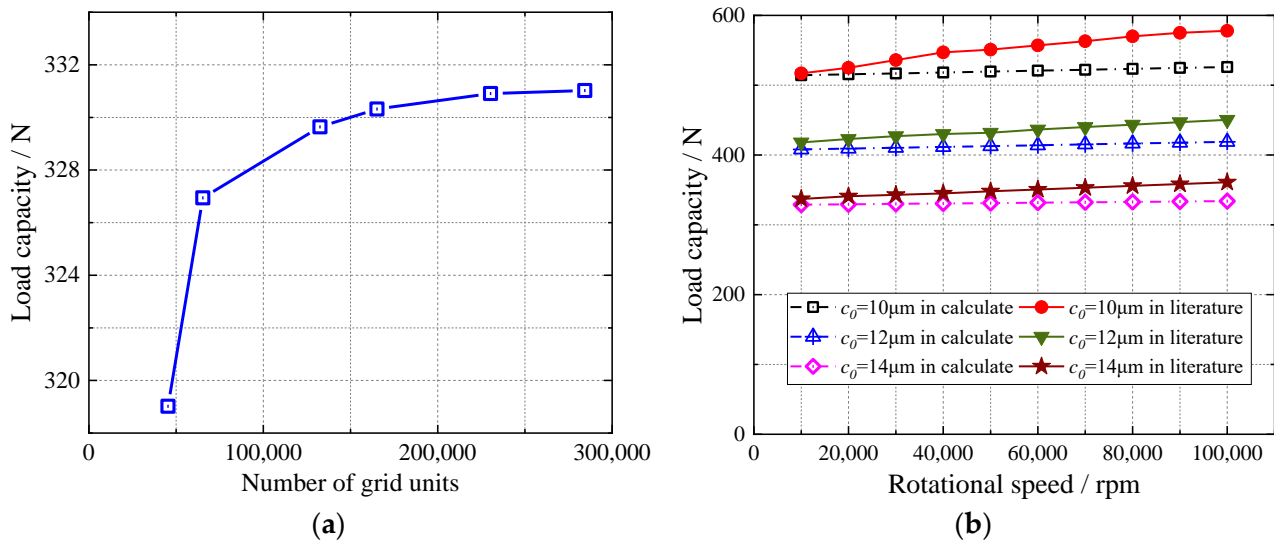


Figure 4. Model verification: (a) grid independence verification and (b) load capacity validation.

Table 1. Bearing parameters from the literature [51] used for validation.

Structural Parameters	Value	Unit
Bearing internal diameter (D_1)	25	mm
Bearing external diameter (D_2)	80	mm
Radius of the orifice circle (R_d)	25	mm
Orifice diameter (d)	0.2	mm
Number of orifices (N)	6	/
Groove depth (h)	0	mm
Groove width (s)	0	mm
Pressure around the bearing (P_0)	101,300	Pa
Supplied pressure (P_{in})	607,800	Pa
Temperature (T)	293	K

3. Influence of Lubricant Properties

Bearing performance is profoundly influenced by the applied gas lubricant. Numerical calculations and comparisons of the static performance of bearings using hydrogen and other common gases have been carried out for a comprehensive understanding of the performance characteristics of HHTBs.

Commonly used gaseous lubricants that have similar physical properties, such as low density and viscosity, can be analyzed according to an identical calculation model. However, in engineering applications, bearings are affected by differences in gaseous physical properties. The density and viscosity of hydrogen are lower compared to those of air, methane and helium, as indicated in Table 2. With a view to investigating the performance characteristics of HHTBs, the above-mentioned lubricating gases were selected for calculation and comparison. The parameters applied in the calculations are presented in Table 3.

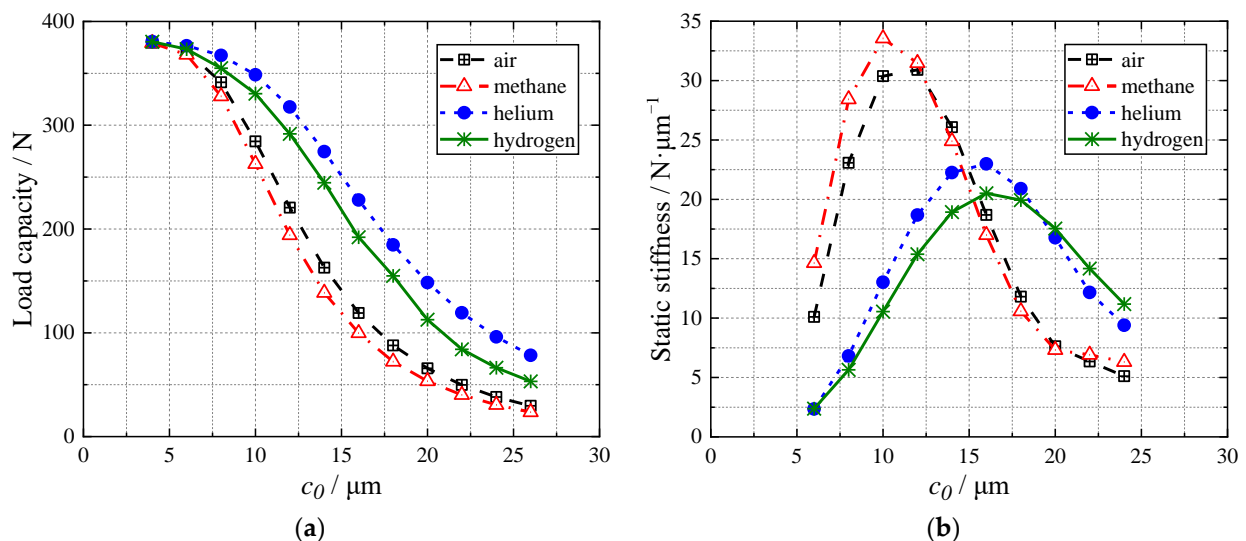
Table 2. Density and viscosity of hydrogen, air, methane and helium at 300 K, 0.5 MPa.

Gas	Density ($\text{kg}\cdot\text{m}^{-3}$)	Viscosity ($\mu\text{Pa}\cdot\text{s}$)
Air	5.8149	18.595
Methane	3.2432	11.189
Helium	0.8004	19.944
Hydrogen	0.4029	8.9407

Table 3. Structural and operational parameters of thrust bearings.

Structural Parameters	Value	Unit
Bearing internal diameter (D_1)	25	mm
Bearing external diameter (D_2)	50	mm
Radius of the orifice circle (R_d)	19	mm
Orifice diameter (d)	0.2	mm
Number of orifices (N)	8	/
Groove depth (h)	0.2	mm
Groove width (s)	0.2	mm
Film clearance (c_0)	10	μm
Pressure around the bearing (P_0)	500,000	Pa
Supplied pressure (P_{in})	1,000,000	Pa
Temperature (T)	293	K
Rotational speed (ω)	50,000	rpm

The static parameters of bearings using different gases are presented in Figure 5. The load capacity of the HHTB was less than that of helium-lubricated bearings but higher than that of air- and methane-lubricated bearings. As film clearance increased, load capacity decreased. Furthermore, the peak static stiffness values of bearings using air and methane were similar and higher than those using helium and hydrogen. Film clearances that corresponded to the peak values for air and methane were smaller than those for helium and hydrogen. With an increment in film clearance, the static stiffness initially increased, then decreased. In general, the HHTB had a significant load capacity, although its stiffness was relatively smaller.

**Figure 5.** Static parameters of bearings using different gases: (a) load capacity and (b) static stiffness.

When the bearing diameters are determined, the load capacity increases as the restrictor coefficient. The throttling coefficient is as follows [20]:

$$\Lambda_s = \frac{6\mu Nd^2 \sqrt{RT}}{P_{in} c_0^3 \sqrt{1 + \delta^2}} \quad (8)$$

where μ is viscosity, N is the number of orifices, d is the orifice diameter, R is the gas constant, P_{in} is supplied pressure and c_0 is film clearance. For the orifice restricted bearing, $\delta = 0$. The restrictor coefficients of helium, hydrogen, air and methane are 29.87, 18.94, 10.35 and 8.38, respectively. This leads to the distribution pattern in the above figure.

The impacts of different gas lubricants on the traces and turbulent kinetic energy in plane B (as displayed in Figure 3) are shown in Figure 6; vortices appear in the circumferential groove. The maximum turbulent kinetic energies of different gas lubricants in ascending order were air, methane, helium and hydrogen. Additionally, the region with high turbulent kinetic energy moved from the center to the wall of the circumferential groove. The turbulence effect of the HHTB was the largest, which may have been caused by its low viscosity.

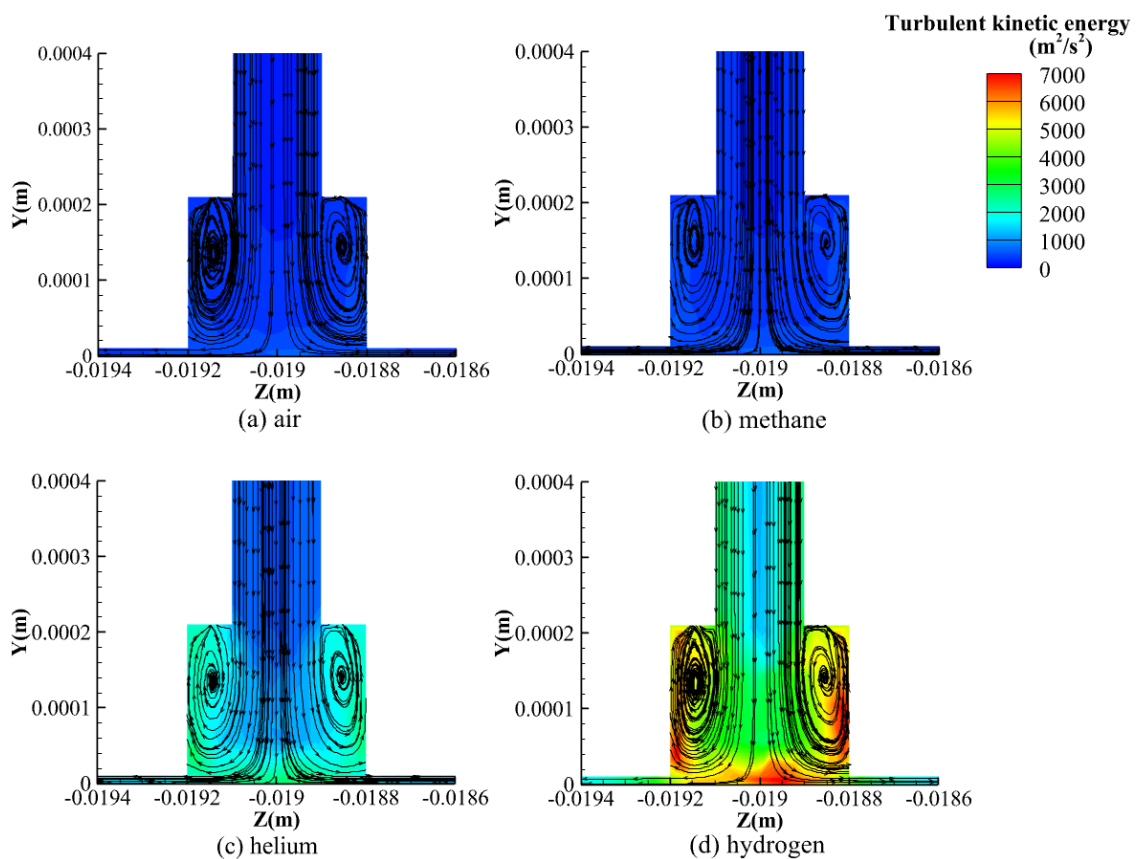


Figure 6. Traces and turbulent kinetic energies of different gas lubricants.

4. Application Parameters

4.1. Supplied Pressure

Increased pressure around the bearings during the start-up of the hydrogen turbo-expander may cause insufficient load capacity of the HHTB during operation. The load capacities of the HHTB under different supplied pressures are presented in Figure 7. Other parameters remained unchanged, as shown in Table 3. Bearing load capacity tended to increase according to the supplied pressure. As the pressure around the bearing increased, the load capacity decreased. Briefly, the benefits of improving the load capacity of the

HHTB were not prominent when the supplied pressure under higher pressure around the bearing was increased.

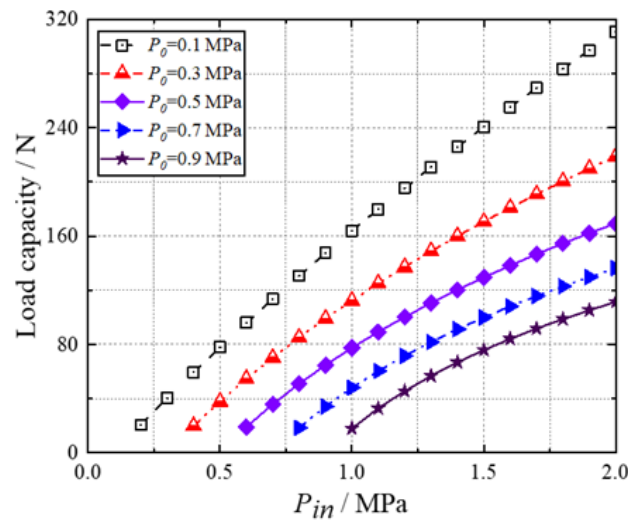


Figure 7. Load capacities of the HHTB under supplied pressures.

4.2. Orifice Diameter

Static parameters with different orifice diameters are presented in Figure 8. Other parameters remained unchanged, as shown in Table 3. Increasing the orifice diameter around the designed orifice value could expand the load capacity. Additionally, the peak value of static stiffness decreased with increases in the orifice diameter. The film clearance corresponding to the peak static stiffness gradually increased with increases in the orifice diameter.

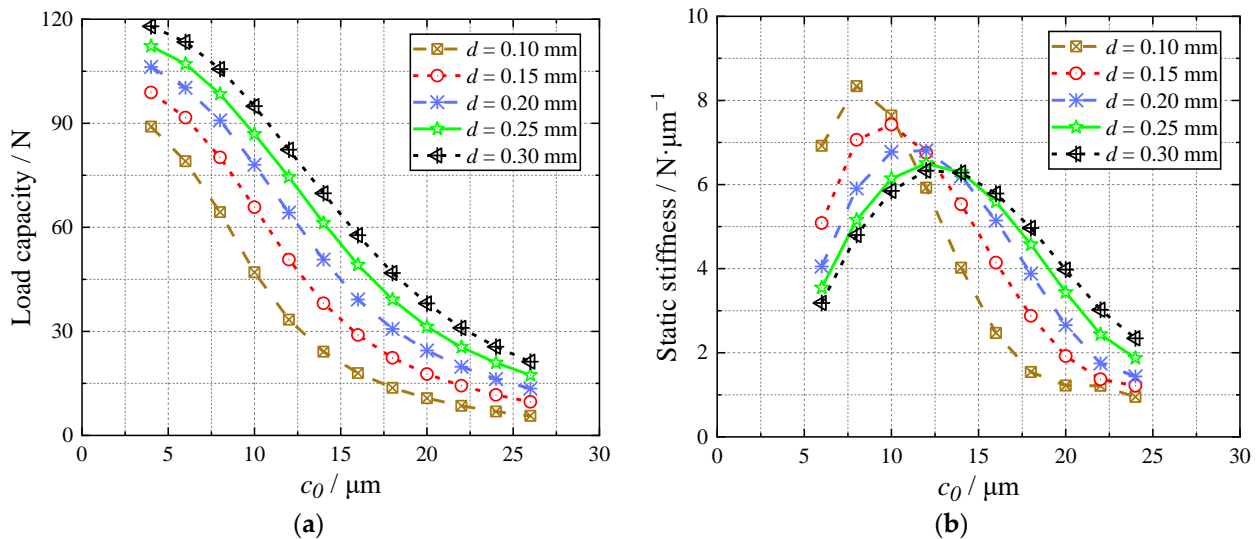


Figure 8. Static parameters of the HHTB with different orifice diameters: (a) load capacity and (b) static stiffness.

4.3. Number of Orifices

The external supplied ability of the HHTB is influenced by the number of supplied orifices. The static parameters of the HHTB using different numbers of orifices are presented in Figure 9. Other parameters remained unchanged, as shown in Table 3. Load capacity and static stiffness were improved by increasing the number of orifices. Moreover, the

film clearance that corresponded to the peak static stiffness rose slightly as the number of orifices increased. Increasing the orifice number boosted bearing performance.

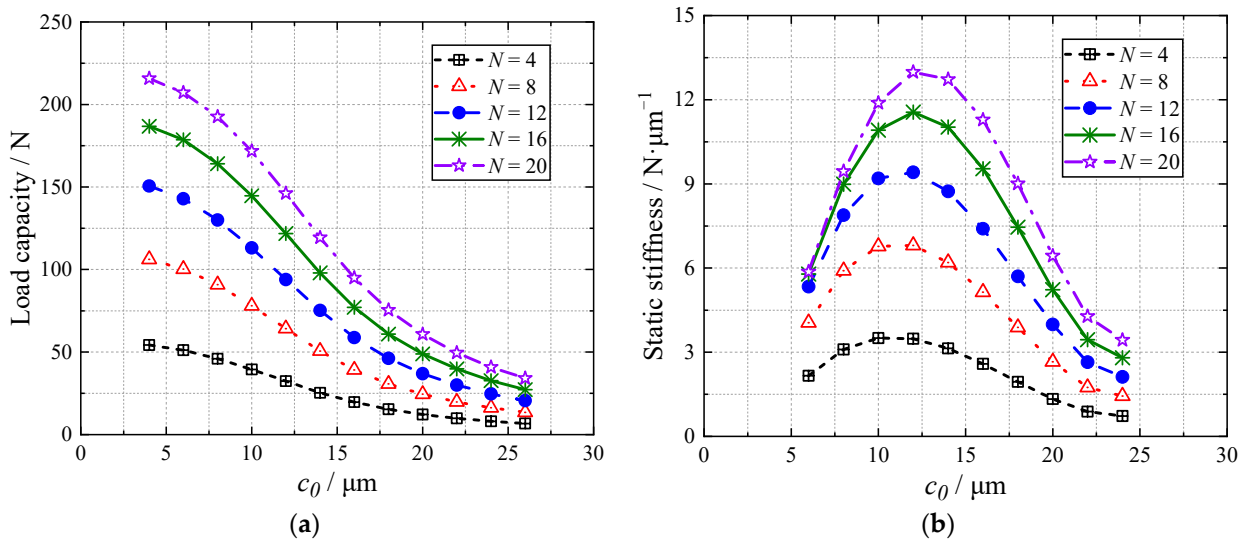


Figure 9. Static parameters of the HHTB using different numbers of orifices: (a) load capacity and (b) static stiffness.

4.4. Circumferential Groove

To improve the performance of the HHTB, a circumferential groove was arranged near the locating circle of the orifice to throttle the gas in the secondary shallow cavity. The static parameters of the HHTB with different groove depths are presented in Figure 10. Other parameters remained unchanged, as shown in Table 3. The bearing with a circumferential groove had a greater load capacity than the bearing without a groove. With deepening grooves, the load capacity of the HHTB gradually increased and tended toward a certain value. Furthermore, the static stiffness of the HHTB was also enhanced after setting a circumferential groove. The film clearance corresponding to the peak static stiffness gradually increased and stabilized with growing circumferential groove depth.

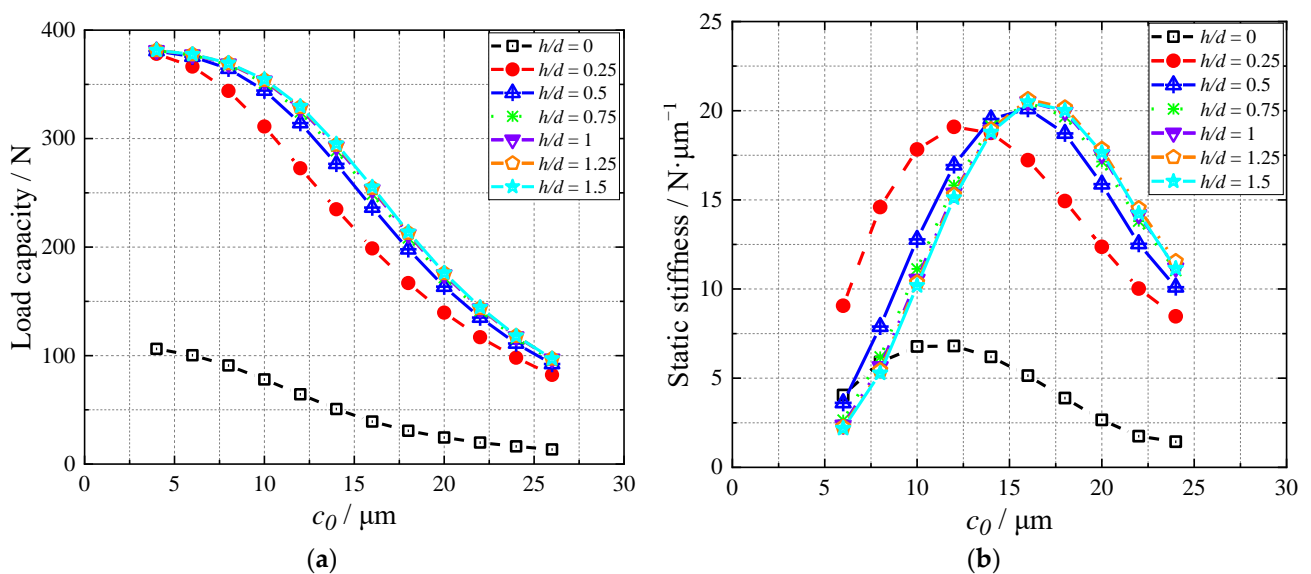


Figure 10. Static parameters of the HHTB under different groove depths: (a) load capacity and (b) static stiffness.

The load capacities of HHTBs for various groove widths are presented in Figure 11. The load capacity of the HHTB initially increased and later decreased as the groove width increased. When the circumferential groove width was small, the load capacity increased because of the increased throttling effect of the shallow secondary cavity. However, the excessive width of the circumferential groove in the later stage was equivalent to increased gas film clearance, which deteriorated the bearing's capacity.

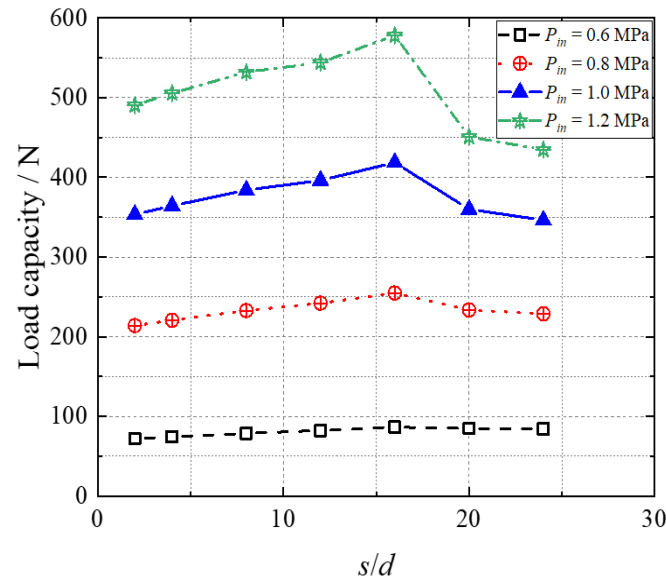


Figure 11. Bearing load capacities for various groove widths ($P_{in} = 1.0$ MPa, $P_0 = 0.5$ MPa).

5. Dynamic Characteristics

Inevitably, the rotor vibrates during this application, which considerably affects the performance of the HHTB. To explore the dynamic characteristics of HHTBs, the effects of harmonic disturbance amplitude, frequency and gas film equilibrium point positions on the dissipated energy, equivalent damping and dynamic stiffness were studied.

Figures 12 and 13 show the load capacity–gas film clearance curve and dynamic parameters of HHTBs for different disturbance amplitudes, disturbance frequencies and gas film equilibrium values. Other parameters remained unchanged, as shown in Table 3. The minimum amounts of bearing load capacity during disturbance decreased with increasing amplitude. As a result, the region enclosed by the load capacity–gas film clearance curve (the dissipated energy) was greater. The dynamic stiffness factor reduced slightly with increasing amplitude. However, the large amplitude led to a low minimum load capacity that did not meet the requirements of this application. The equivalent damping of the HHTB varied irregularly with disturbance amplitude. The counterclockwise load capacity–film clearance curve shows that the positive damping dissipated the system disturbance energy and improved reliability [35].

The maximum and minimum load capacity values were almost identical at different disturbance frequencies. The dissipation energy of the HHTB increased as the disturbance frequency increased. The dynamic stiffness and equivalent damping of the HHTB decreased as the disturbance frequency increased.

The increase in the film equilibrium value caused a decrease in the overall load capacity. In addition, the dissipated energy and equivalent damping of the HHTB decreased as the air film equilibrium value increased. The dynamic stiffness of the bearing increased and then decreased.

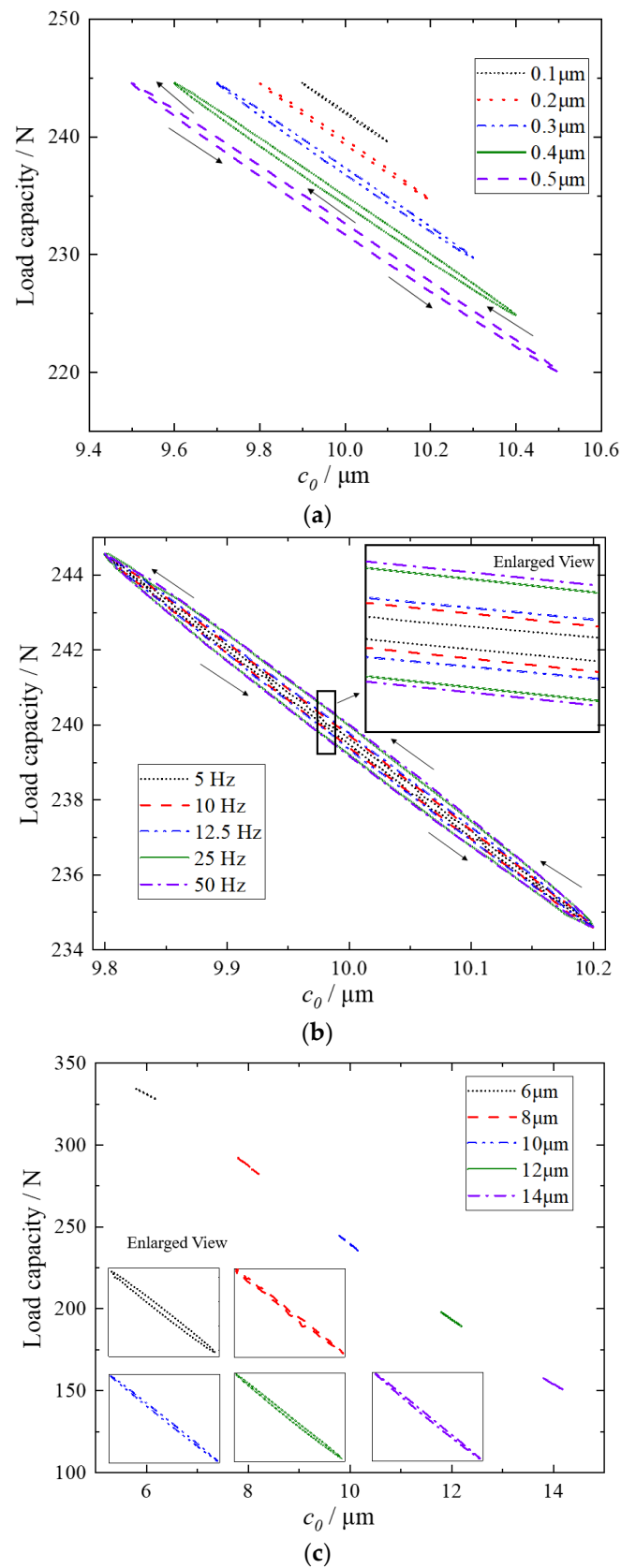


Figure 12. Variation in dynamic load capacity at (a) different amplitudes, (b) different frequencies and (c) different film equilibrium values.

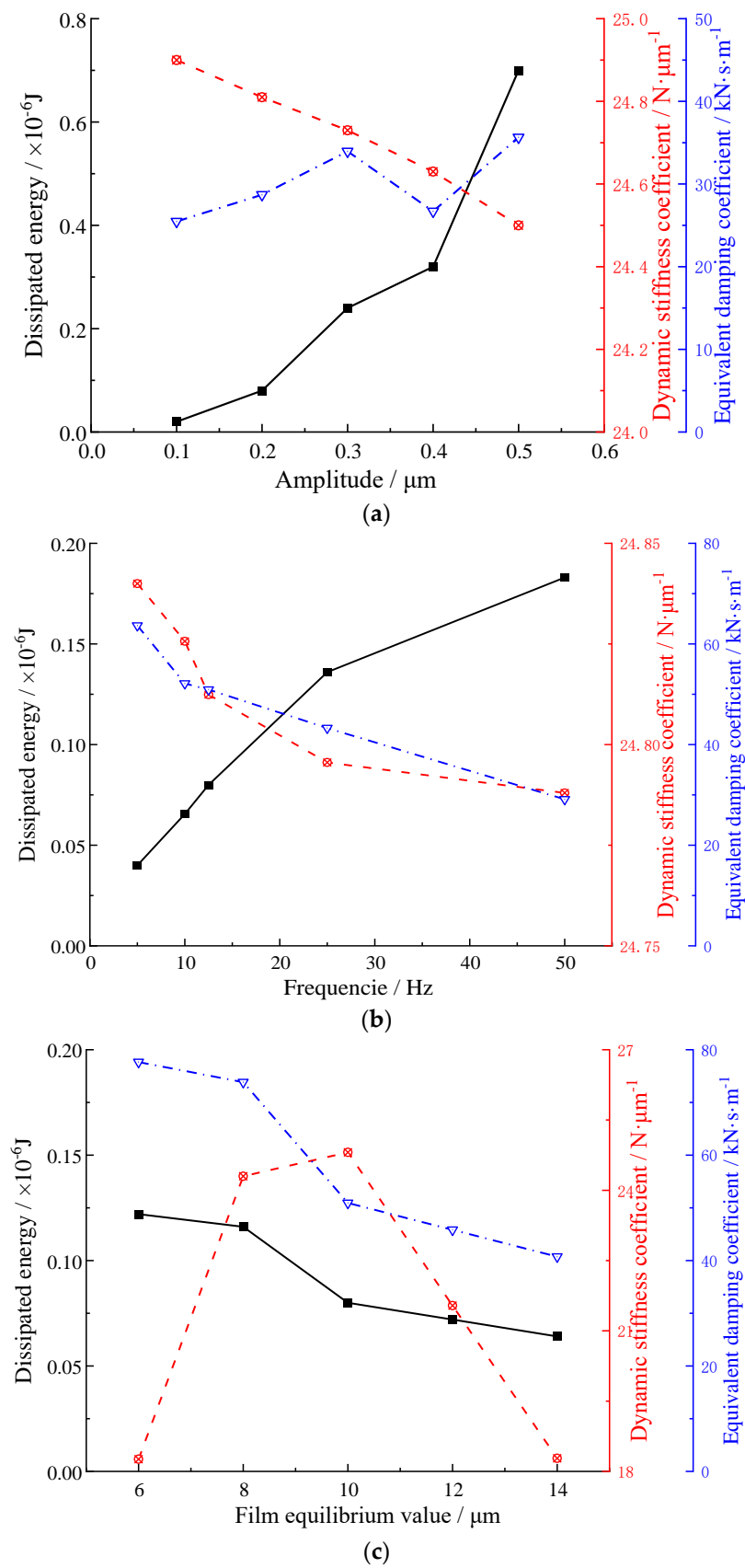


Figure 13. Variation in dynamic parameters of HHTBs at (a) different amplitudes, (b) different frequencies and (c) different film equilibrium values.

6. Conclusions

To explore the feasibility of using HHTBs in hydrogen liquefaction applications, the performance of HHTBs was simulated and compared with that of bearings using air, helium and methane as lubricants. The impacts of gas-supplied pressure, orifice diameter, orifice quantity, circumferential groove and film clearance on bearing performances were considered. Dynamic characteristics of HHTBs under harmonic disturbance were studied using the dynamic grid method. Conclusions obtained from calculations and the analysis of results are especially useful as a design guide for HHTBs, as follows:

- Bearing performance is strongly influenced by gaseous physical properties. The four gas-lubricated bearings have load capacities in the following order: helium, hydrogen, air and methane. The peak values of stiffness of bearings, in descending order, are those of methane, air, helium and hydrogen. Hydrogen has the highest turbulent kinetic energy. In a word, HHTBs can provide considerable load capacity in this application.
- Effective methods for enhancing the bearing load capacity of HHTBs include elevating the gas-supplied pressure under constant pressure around the bearing, appropriately expanding the orifice diameter, augmenting the number of gas supply orifices, reducing gas film clearance and setting circumferential grooves.
- When the amplitude of harmonic disturbance increases, the bearing's dynamic stiffness decreases, resulting in better dynamic stability; however, the minimum bearing capacity may be lower. The harmonic disturbance frequency has a small effect on the dynamic stiffness, within a certain range. For the same disturbance, a smaller value of gas film balance increases the equivalent damping and dynamic stiffness of the HHTB.

In summary, HHTBs are not inferior to commonly used air bearings in terms of load capacity, and have good stiffness at higher clearances; therefore, they can be used on hydrogen turbo-machinery.

Author Contributions: Conceptualization, M.Q. and T.L.; methodology, M.Q.; software, M.Q.; validation, M.L. and S.Y.; formal analysis, Q.Z.; resources, S.Y.; data curation, M.Q.; writing—original draft preparation, M.Q.; writing—review and editing, Y.H. and T.L.; supervision, Y.H. and T.L.; project administration, Y.H. and T.L.; funding acquisition, T.L. All authors have read and agreed to the published version of the manuscript.

Funding: This project was funded by the National Key R&D Program of China (2022YFB3402700), the National Natural Science Foundation of China (51976150) and the Youth Innovation Team of Shaanxi Universities.

Institutional Review Board Statement: This study did not involve humans or animals.

Informed Consent Statement: This study did not involve humans or animals.

Data Availability Statement: This study did not report any data.

Acknowledgments: The authors give their thanks for the support of the National Key R&D Program of China (2022YFB3402700), the National Natural Science Foundation of China (51976150) and the Youth Innovation Team of Shaanxi Universities.

Conflicts of Interest: The authors declare no conflict of interest.

References

1. Midilli, A.; Ay, M.; Dincer, I.; Rosen, M.A. On hydrogen and hydrogen energy strategies I: Current status and needs. *Renew. Sustain. Energy Rev.* **2005**, *9*, 255–271. [[CrossRef](#)]
2. Sherif, S.A.; Barbir, F.; Veziroglu, T.N. Wind energy and the hydrogen economy—Review of the technology. *Sol. Energy* **2005**, *78*, 647–660. [[CrossRef](#)]
3. Meng, N.; Yu, X.; Liu, F.; Zhao, P.; Zhao, B. Influences of renewable energy on hydrogen storage system and its control strategy. *Electr. Power Constr.* **2018**, *39*, 28–34. [[CrossRef](#)]
4. Song, J.; Zhu, Y.; Liang, D.; Cheng, Q.; Bao, W. Hydrogen energy system for renewable energy consumption. *E3S Web Conf.* **2021**, *233*, 01083.

5. Afanasiev, A.N.; Pavlov, D.A.; Epishkin, V.E.; Gapchenko, U.A. Application of hydrogen and hydrogen-containing gases in internal combustion engines. *IOP Conf. Ser. Mater. Sci. Eng.* **2020**, *734*, 012198. [[CrossRef](#)]
6. Manoharan, Y.; Hosseini, S.E.; Butler, B.; Alzahrani, H.; Krohn, J. Hydrogen fuel cell vehicles; current status and future prospect. *Appl. Sci.* **2019**, *9*, 2296. [[CrossRef](#)]
7. Liu, M.; Zhang, L.; Little, M.A.; Kapil, V.; Ceriotti, M.; Yang, S. Barely porous organic cages for hydrogen isotope separation. *Science* **2019**, *366*, 613–620. [[CrossRef](#)]
8. Ma, L.T.; Chen, S.M.; Li, N.; Liu, Z.X.; Tang, Z.J.; Zapien, J.A.; Chen, S.; Fan, J.; Zhi, C. Hydrogen-Free and Dendrite-Free All-Solid-State Zn-Ion Batteries. *Adv. Mater.* **2020**, *32*, 1908121. [[CrossRef](#)]
9. Midilli, A.; Dincer, I. Key strategies of hydrogen energy systems for sustainability. *Int. J. Hydrog. Energy* **2006**, *32*, 511–524. [[CrossRef](#)]
10. Barthelemy, H.; Weber, F.; France, B. Hydrogen storage: Recent improvements and industrial perspectives. *Int. J. Hydrog. Energy* **2016**, *42*, 7254–7262. [[CrossRef](#)]
11. Rivard, E.; Trudeau, M.; Zaghbi, K. Hydrogen storage for mobility: A review. *Materials* **2019**, *12*, 1973. [[CrossRef](#)]
12. Elberry, A.M.; Thakur, J.; Santasalo-Aarnio, A.; Larmi, M. Large-scale compressed hydrogen storage as part of renewable electricity storage systems. *Int. J. Hydrog. Energy* **2021**, *46*, 15671–15690. [[CrossRef](#)]
13. Krasae-In, S.; Stang, J.H.; Neksa, P. Development of large-scale hydrogen liquefaction processes from 1898 to 2009. *Int. J. Hydrog. Energy* **2010**, *35*, 4524–4533. [[CrossRef](#)]
14. Mehta, M.; Zaaijer, M.; Von Terzi, D. Optimum Turbine Design for Hydrogen Production from Offshore Wind. *J. Phys. Conf. Ser.* **2022**, *2265*, 042061. [[CrossRef](#)]
15. Lim, H.; Seo, J.; Park, M.; Choi, B.; Park, J.; Bang, J. A Numerical Study on Blade Design and Optimization of a Helium Expander for a Hydrogen Liquefaction Plant. *Appl. Sci.* **2022**, *3*, 1411. [[CrossRef](#)]
16. Davydov, A.B.; Perestoronin, G.A. Turbine Expanders in Hydrogen Liquefiers. *Chem. Pet. Eng.* **1997**, *33*, 174–177. [[CrossRef](#)]
17. Yan, H.; Ke, C.L.; Peng, N.; Li, K.R.; Zhang, X.H.; Zheng, L.W.; Liang, Y.W.; Xiong, L.Y.; Dong, B.; Li, J.; et al. Static and dynamic characteristics of externally pressurized gas bearing for high-speed hydrogen turbo-expander. *IOP Conf. Ser. Mater. Sci. Eng.* **2022**, *1240*, 012114. [[CrossRef](#)]
18. Bischoff, S.; Decker, L. First operating results of a dynamic gas bearing turbine in an industrial hydrogen liquefier. *Am. Inst. Phys.* **2010**, *1218*, 887–894. [[CrossRef](#)]
19. Davydenkov, A.I.; Ravikovitch, A.Y.; Davydov, B.A.; Yu, I. Development of cryogenic turboexpanders with gas dynamic foil bearings. *Cryogenics* **1992**, *32*, 80–83. [[CrossRef](#)]
20. Institute, R.P.; Wilcock, D.F.; Sandor, G.N. *Design of Gas Bearings: Notes Supplemental to the RPI-MTI Course on Gas Bearing Design, 14–18 August 1967*; Rensselaer Polytechnic Institute: Troy, NY, USA; Mechanical Technology Inc.: Helena, MT, USA, 1967.
21. Yoshimoto, S. Trends in gas bearings. *Jpn. J. Tribol.* **1997**, *42*, 1415–1417.
22. Mizumoto, H. A fascinating world of hydrostatic and aerostatic bearings. *J. Jpn. Soc. Precis. Eng.* **2007**, *73*, 537–540. [[CrossRef](#)]
23. Majumdar, B.C. Gas-lubricated porous bearings: A bibliography. *Wear* **1976**, *36*, 269–273. [[CrossRef](#)]
24. Chen, S.; Zhang, Q.; Fu, B.; Liu, Z.; Li, S. Analysis of static and dynamic characteristics of aerostatic bearing with reflux orifices. *Ind. Lubr. Tribol.* **2021**, *73*, 961–970.
25. Kwan, Y.; Corbett, J. Porous aerostatic bearings—an update review. *Wear* **1998**, *222*, 69–73. [[CrossRef](#)]
26. Gao, Q.; Chen, W.Q.; Lu, L.H.; Huo, D.H.; Cheng, K. Aerostatic bearings design and analysis with the application to precision engineering: State-of-the-art and future perspectives. *Tribol. Int.* **2019**, *135*, 1–17. [[CrossRef](#)]
27. Miyatake, M.; Yoshimoto, S. Numerical investigation of static and dynamic characteristics of aerostatic thrust bearings with small feed holes. *Tribol. Int.* **2010**, *43*, 1353–1359. [[CrossRef](#)]
28. Nishio, U.; Somaya, K.; Yoshimoto, S. Numerical calculation and experimental verification of static and dynamic characteristics of aerostatic thrust bearings with small feedholes. *Tribol. Int.* **2011**, *44*, 1790–1795. [[CrossRef](#)]
29. Gao, S.; Cheng, K.; Chen, S.; Ding, H.; Fu, H. CFD based investigation on influence of orifice chamber shapes for the design of aerostatic thrust bearings at ultra-high speed spindles. *Tribol. Int.* **2015**, *92*, 211–221. [[CrossRef](#)]
30. Renn, J.C.; Hsiao, C.H. Experimental and CFD study on the mass flow-rate characteristic of gas through orifice-type restrictor in aerostatic bearings. *Tribol. Int.* **2004**, *37*, 309–315. [[CrossRef](#)]
31. Shi, J.; Cao, H.; Maroju, N.K.; Jin, X. Dynamic modeling of aerostatic spindle with shaft tilt deformation. *J. Manuf. Sci. Eng.* **2019**, *142*, 1–43. [[CrossRef](#)]
32. Li, Y.; Xin, W.; Sun, Z.; Sun, W.; Li, X. A Calculation Method for the Micro-vibration Amplitude of an Aerostatic Thrust Bearing and the Influence of Bearing Parameters on the Vibration. In Proceedings of the 5th International Conference on Measurement, Instrumentation and Automation (ICMIA 2016), Shenzhen, China, 17–18 September 2016.
33. Zhao, X.; Zhang, J.; Dong, H.; Fang, Z.; Li, J. Numerical simulation and experimental study on the gas-solid coupling of the aerostatic thrust bearing with elastic equalizing pressure groove. *Shock. Vib.* **2017**, *2017*, 1–11.
34. Huang, T.; Weng, S.; Hsu, S. Effect of variation of gap thickness of the thrust bearing on gap pressure and stiffness of the aerostatic spindle in vertical milling. *Key Eng. Mater.* **2017**, *739*, 1–6. [[CrossRef](#)]
35. Zheng, Y.; Yang, G.; Cui, H.; Hou, Y. Pneumatic stability analysis of single-pad aerostatic thrust bearing with pocketed orifice. *Arch. Proc. Inst. Mech. Eng. Part J J. Eng. Tribol.* **2019**, *234*, 135065011989416. [[CrossRef](#)]

36. Wu, Y.; Li, C.; Du, J.; Liu, T.; Zuo, X. Pneumatic hammer characteristics of the aerostatic thrust bearing with central orifice and pressure-equalizing groove. *Nonlinear Dyn.* **2023**, *111*, 2161–2182. [[CrossRef](#)]
37. Sahto, M.P.; Wang, W.; Sanjrani, A.N.; Hao, C.X.; Shah, S.A. Dynamic performance of partially orifice porous aerostatic thrust bearing. *Micromachines* **2021**, *12*, 989. [[CrossRef](#)]
38. Wei, L.; Gang, B. Improvement of load capacity of circular aerostatic thrust bearings with the finite volume method. In Proceedings of the IEEE International Conference on Automation & Logistics, Qingdao, China, 1–3 September 2008.
39. Ishibashi, K.; Kondo, A.; Kawada, S.; Miyatake, M.; Yoshimoto, S.; Stolarski, T. Static and dynamic characteristics of a downsized aerostatic circular thrust bearing with a single feed hole. *Precis. Eng.* **2019**, *60*, 448–457. [[CrossRef](#)]
40. Guo, Y.; Lai, T.; Ren, X.; Zhao, Q.; Hou, Y. Effect of lubrication medium on gas bearing performance. *Lubr. Eng.* **2021**, *46*, 1–5.
41. Yan, H.; Ke, C.; Peng, N.; Li, K.; Zhang, X.; Xiong, L.; Dong, B.; Li, J.; Liu, L. Performance prediction of externally pressurized gas bearings for high-speed turbo-expander involving hydrogen, helium and air working fluids—ScienceDirect. *Int. J. Hydrog. Energy* **2021**, *46*, 33453–33467. [[CrossRef](#)]
42. Raparelli, T.; Viktorov, V.; Colombo, F.; Lentini, L. Aerostatic thrust bearings active compensation: Critical review. *Precis. Eng.* **2016**, *44*, 1–12. [[CrossRef](#)]
43. Chen, X.D.; Zhu, J.C.; Chen, H. Dynamic characteristics of ultra-precision aerostatic bearings. *Adv. Manuf.* **2013**, *1*, 82–86. [[CrossRef](#)]
44. Lo, C.Y.; Wang, C.C.; Lee, Y.H. Performance analysis of high-speed spindle aerostatic bearings. *Tribol. Int.* **2005**, *38*, 5–14. [[CrossRef](#)]
45. Li, Y.; Han, D. Influences of the geometrical parameters of aerostatic thrust bearing with pocketed orifice-type restrictor on its performance. *Tribol. Int.* **2007**, *40*, 1120–1126. [[CrossRef](#)]
46. Cheng, K.; Rowe, W.B. A selection strategy for the design of externally pressurized journal bearings. *Tribol. Int.* **1995**, *28*, 465–474. [[CrossRef](#)]
47. Gu, L.; Guenat, E.; Schiffmann, J. A review of grooved dynamic gas bearings. *Appl. Mech. Rev.* **2020**, *72*, 15. [[CrossRef](#)]
48. Lin, Y.; Noah, S. Using Genetic Algorithms for the Optimal Design of Fluid Journal Bearing. In Proceedings of the ASME 1999 Design Engineering Technical Conferences, Las Vegas, NV, USA, 12–15 September 1999.
49. Zhang, Q.; Gao, M.; Xu, H.; Fu, Y.; Duan, J. Theoretical and experimental study on the dynamic characteristics of tilting pad thrust bearing considering excitation frequency. *J. Mech. Eng.* **2014**, *50*, 50–58. [[CrossRef](#)]
50. Zhao, Q.; Qiang, M.; Yan, S.; Liu, X.; Hou, Y.; Lai, T. Frictional analysis on stiffness and damping characteristics of bump foil gas bearings. *Proc. Inst. Mech. Eng. Part J J. Eng. Tribol.* **2022**, *237*, 498–513. [[CrossRef](#)]
51. Shi, J.; Cao, H.; Jin, X. Investigation on the static and dynamic characteristics of 3-DOF aerostatic thrust bearings with orifice restrictor. *Tribol. Int.* **2019**, *138*, 435–449. [[CrossRef](#)]

Disclaimer/Publisher’s Note: The statements, opinions and data contained in all publications are solely those of the individual author(s) and contributor(s) and not of MDPI and/or the editor(s). MDPI and/or the editor(s) disclaim responsibility for any injury to people or property resulting from any ideas, methods, instructions or products referred to in the content.